Applying InSAR and GNSS Data to Obtain 3-D Surface Deformations Based on Iterated Almost Unbiased Estimation and Laplacian Smoothness Constraint

Panfeng Ji, Xiaolei Lv, *Member, IEEE*, Qi Chen, Guangcai Sun, *Senior Member, IEEE*, and Jingchuan Yao

***Abstract*—Global navigation satellite system (GNSS) and interferometric synthetic aperture radar (InSAR) data are integrated to extract the 3-D surface deformations, which are of great significance for studying geological hazards. In this study, two major problems are focused on integration. For one thing, we propose an iterated almost unbiased estimation (IAUE) method to estimate the variance components of GNSS and InSAR for the case where the estimation of variance components of multisource data by traditional variance component estimation methods may be negative and inaccurate. For another, considering that heterogeneous data errors may lead to unstable 3-D solutions, we propose adding the Laplacian smoothness constraint (LSC) to the function model, which can smooth the solutions by minimizing the second derivative of the displacements. These two methods are abbreviated as IAUE-LSC. In the simulation experiment, the performance of traditional Helmert variance component estimation is first compared with IAUE. IAUE can not only converge more quickly, but also avoid negative variances. Furthermore, we find that the excessively large relative error ratio between GNSS and InSAR is an essential factor leading to the instability of the 3-D solutions. The IAUE-LSC method is immune to this instability and can obtain more stable results. In addition, the 2018 Hawaii case demonstrates that IAUE achieves improvements of 2.58, 2.77, and 7.69 cm in the east, north, and up directions relative to the traditional weighted least-squares method, while the combined IAUE-LSC achieves improvements of 2.29, 0.32, and 1.68 cm compared to the IAUE alone.**

***Index Terms*—Global navigation satellite system (GNSS), interferometric synthetic aperture radar (InSAR), iterated almost unbiased estimation (IAUE), Laplacian smoothness constraint (LSC), variance component estimation (VCE), 3-D.**

Manuscript received May 10, 2020; revised July 22, 2020 and November 3, 2020; accepted November 19, 2020. Date of publication November 24, 2020; date of current version January 6, 2021. This work was supported in part by the National Key R&D Program of China under Grant 2018YFC1505100, in part by the China Academy of Railway Sciences Fund under Grant 2019YJ028, and in part by the Key R&D Program of Shaanxi under Grant 2019ZDLGY08-05. *(Corresponding author: Xiaolei Lv.)*

Panfeng Ji and Xiaolei Lv are with the Key Laboratory of Technology in Geo-Spatial Information Processing and Application System, Aerospace Information Research Institute, Chinese Academy of Sciences, Beijing 100094, China, and also with the School of Electronic, Electrical, and Communication Engineering, University of Chinese Academy of Sciences, Beijing 100049, China (e-mail: jipanfeng17@mails.ucas.ac.cn; academism2017@sina.com).

Qi Chen is with the China Center for Resources Satellite Data and Application, Beijing 100094, China (e-mail: chenq_cn@163.com).

Guangcai Sun is with the National Laboratory of Radar Signal Processing, Xidian University, Xi'an 710071, China (e-mail: gcsun@xidian.edu.cn).

Jingchuan Yao is with the State Key Laboratory of High Speed Railway Track Technology, China Academy of Railway Sciences, Beijing 100891, China (e-mail: yjcwxj@rails.cn).

Digital Object Identifier 10.1109/JSTARS.2020.3040317

I. Introduction

INTERFEROMETRIC synthetic aperture radar (InSAR) and global navigation satellite system (GNSS) have been proven to be useful tools for high-precision surface deformation monitoring [1]. However, both of them have insurmountable shortcomings. On the one hand, InSAR can obtain spatially continuous deformation, but it is only 1-D (in the direction of the line of sight, LOS). On the other hand, the GNSS can acquire high-precision 3-D displacements, but it is spatially discrete [2]. Obviously, they are highly complementary and can be combined to obtain high-precision 3-D deformation maps.

To obtain 3-D surface deformations, one method is to interpolate sparse GNSS points to the same spatial lattice of the InSAR [3], and the other is to use InSAR observations from different satellites or different techniques, such as multiple aperture interferometry (MAI) and offset tracking, and then construct a 3-D optimization equation group [4]. Compared with the latter, the former can make up for the low accuracy of InSAR observation in the north–south direction, although it may lead to errors caused by the interpolation of GNSS points. The principle of both methods is based on the weighted least-squares (WLS) method, so the weights of the different observations, or the variance/covariance matrix, must be considered first [5]. In the past, *a priori* weighting method was often used. The standard deviation of GNSS observation was obtained by interpolating the positioning error to synthesize the positioning and interpolation errors [3]. There are two most widely used methods for calculating InSAR standard deviation. One is based on coherence calculation [6]

$$\sigma_{\text{los}} = \frac{1}{\sqrt{2N_l}} \times \frac{\sqrt{1-\gamma^2}}{\gamma} \tag{1}$$

where N_l is the number of looks and γ is the absolute value of coherence for two synthetic aperture radar (SAR) images. The other is the window sliding method [7], that is, setting a regular window in the SAR image centering on the estimated observation point, and assuming that the observations of all points in the window follow the same process, the standard

deviation of the observation point can be approximated by

$$\sigma_{\text{los}} = \sqrt{\frac{\sum_N (D(i,j) - \bar{D}(i,j))^2}{N-1}} \tag{2}$$

where $D(i,j)$ is the displacement observation of the corresponding observation point in the window, $\bar{D}(i,j)$ is the average value of the deformation observation of all points in the window, and N is the number of pixels in the window. An *a priori* weighting method has been used many times to obtain the optimal 3-D results, such as the analytical optimization method [3], the BFGS method [8], the ant colony optimization method [9], the MRF-L1 regularization [2], etc. The *a priori* method may be reasonable in a sense, but it is not accurate. On the one hand, it is difficult to calculate the real InSAR standard deviation only by coherence [10]. On the other hand, the accuracy of GNSS standard deviation interpolation method is often questioned [11].

Since then, some methods using the posterior variance component estimation (VCE) have been continuously studied. The Helmert variance component estimation (HVCE) method was applied to estimate the variance components of GNSS and InSAR by Hu *et al.* [11] and InSAR and MAI by Liu *et al.* [4]. Moreover, a VCE method based on the least-squares (LS) criterion called LS-VCE [12] was used to obtain the variance components of different InSAR observations [13]. However, traditional VCE methods require large computational resources and sometimes produce negative estimates [14]. The reasons for negative variances are complex and cannot be explained physically, although they can still be used to obtain purely mathematical 3-D solutions. Song *et al.* [15] proposed the best quadratic unbiased estimator method to try to solve this problem, but it is under the assumption of the Gauss–Helmert model, which lacks practicality. Amiri-Simkooei [16] proposed a method called NNLS-VCE using the well-known principle of the LS subject to the nonnegativity constraints to avoid the generation of negative variances. However, it not only increases the computational complexity due to the introduction of nonlinearity, but also produces zero variance, which is unacceptable considering that the inverse of the variance matrix will be used as the weights of the observations.

In addition, integration of GNSS with InSAR is often a large-scale ill-conditioned inverse problem due to different sources of errors from heterogeneous data [17]. Traditional VCE can only obtain the variance components of InSAR deformation rate by relying on a large number of SAR interference pairs to increase redundancy, but cannot estimate the variance components of InSAR displacements extracted from two SAR images [11]. To solve this problem, Liu *et al.* [4] proposed the SM-VCE method to combine the observations of the pixels around the target point through spatial correlation to increase the redundancy. However, this combination method makes the design matrix very huge and is easy to produce complex collinear phenomena, thereby aggravating the ill-posed problems of the system itself. This causes the numerical instability of the optimal solutions, which needs to be handled appropriately.

In response to the above problems, on the one hand, we propose an iterated almost unbiased estimation (IAUE) method to obtain the variance components of data sources such as GNSS and InSAR. IAUE provides a biased estimator, but it can converge to an approximately unbiased point through multiple iterations. The advantages of the IAUE method are that it never produces negative variance components, demands less computational resources, and converges much more quickly than other VCE approaches [18]. On the other hand, we propose to use the Laplacian smoothness constraint (LSC) to modify the traditional function model by adding conditions that limit the displacement changes between adjacent pixels. It can stabilize the ill-conditioned models with a special regularization method. In addition, discrete GNSS points will be expanded to the same resolution as InSAR, using the grid strain method [19] instead of the traditional Kriging interpolation [3]. We will first conduct a simulation experiment and then further verify the proposed method's effectiveness through the real case of the 2018 Hawaii earthquakes.

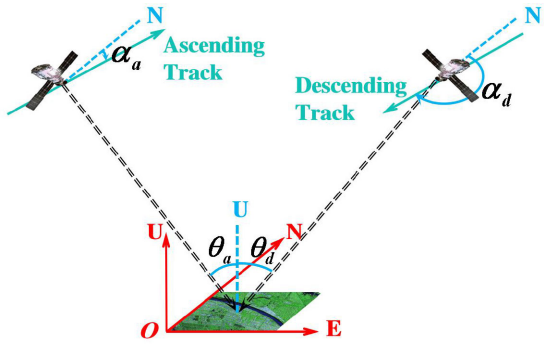

Fig. 1. Geometric relationship between the ascending and descending track InSAR and the real 3-D surface deformations.

II. Methods

A. Optimization Model

1-D surface deformation d_{los} in the LOS direction can be obtained by using differential InSAR. In theory, to derive deformations in the east (d_e), north (d_n), and up (d_u) directions, we need to combine other geodetic data such GNSS [5]. Fig. 1 shows the geometric relationship between ascending and descending InSAR tracks and true 3-D surface deformations. d_{los} can be expressed by the three components as follows:

$$d_{\text{los}} = [s_e \ s_n \ s_u][d_e \ d_n \ d_u]^T \tag{3}$$

where the unit project vector $[s_e \ \ s_n \ \ s_u] = [-\sin\theta\sin(\alpha - 3/2\pi) \ \ -\sin\theta\cos(\alpha - 3/2\pi) \ \ \cos\theta]$, θ is the incidence angle of satellite sight, and α is the heading angle, that is, the clockwise angle between the north and the flight of the satellite. In order to combine InSAR and GNSS data to obtain 3-D surface deformations, discrete GNSS points need to be interpolated to the same position as InSAR.

InSAR and the interpolated GNSS observations can then be combined to derive the final 3-D displacement maps. The process of solving the 3-D optimal solutions can be expressed as a linear

model, which contains the functional part

$$E\{y\} = A_g \cdot d \tag{4}$$

and the stochastic part

$$D\{y\} = Q_y = \sum_{i=1}^{k} \sigma_i^2 Q_i \tag{5}$$

where $E\{\cdot\}$ and $D\{\cdot\}$ denote the expectation operator and the dispersion operator, respectively. $y = [y_{ge}\ y_{gn}\ y_{gu}\ y_{ia}\ y_{id}]^T$ indicates the observation vector, which contains the GNSS east (y_{ge}), north (y_{gn}), and up (y_{gu}) components and the InSAR ascending (y_{ia}) and descending (y_{id}) orbit components. $d = [d_e\ d_n\ d_u]^T$ represents the unknown 3-D deformations vector. Q_i is the known co-factor matrix of observations and σ_i^2 refers to the unknown variance components. k indicates the number of groups into which observations are divided. The design matrix A_g is represented as follows:

$$A_g = \begin{bmatrix} 1 & 0 & 0 \\ 0 & 1 & 0 \\ 0 & 0 & 1 \\ s_e^a & s_n^a & s_u^a \\ s_e^d & s_n^d & s_u^d \end{bmatrix} \tag{6}$$

where superscripts a and d indicate the ascending and descending orbits, respectively.

B. Grid Strain Model

Before introducing IAUE-LSC, we will once again elaborate on the important method of the grid strain model in this section. The grid strain model plays two roles in our processing strategy: one is to extend the displacements of discrete GNSS points to the same resolution grid as InSAR [20], [21], and the other is to combine the surrounding observation points to increase the redundancy of VCE [4].

In a grid image of size $M \times N$, we suppose that the 3-D position vector of the target point P_0 is $p_0 = [p_{0e}\ p_{0n}\ p_{0u}]^T$, and the deformation vector is $d_0 = [d_{0e}\ d_{0n}\ d_{0u}]^T$. There are N surrounding experimental points (EPs) whose positions and displacements are $p_i = [p_{ie}\ p_{in}\ p_{iu}]^T$ and $d_i = [d_{ie}\ d_{in}\ d_{iu}]^T (i = 1, 2, \ldots, N)$, respectively. Based on the stain model theory, they can be modeled as N equations

$$d_i = H \triangle p_i + d_0, \quad i = 1, 2, \ldots, N \tag{7}$$

where $\triangle p_i = p_i - p_0$ represents the position difference vector from the ith EP P_i to the target point P_0. H denotes the stain parameter matrix and can be divided into a strain tensor component E_s

$$E_s = \frac{1}{2}(H_{ij} + H_{ji}) e_i \otimes e_j = \begin{bmatrix} \epsilon_{11} & \epsilon_{12} & \epsilon_{13} \\ \epsilon_{21} & \epsilon_{22} & \epsilon_{23} \\ \epsilon_{31} & \epsilon_{32} & \epsilon_{33} \end{bmatrix} \tag{8}$$

and a rigid body tensor component Ω_s

$$\Omega_s = \frac{1}{2}(H_{ij} - H_{ji}) e_i \otimes e_j = \begin{bmatrix} 0 & -\omega_3 & \omega_2 \\ \omega_3 & 0 & -\omega_1 \\ -\omega_2 & \omega_1 & 0 \end{bmatrix} \tag{9}$$

where $\epsilon_{\{\cdot\}}$ and $\omega_{\{\cdot\}}$ are the parameters of stain model, e_i is the canonical base vector of the Cartesian reference system, and $\otimes$ is the tensor product. In a compact form, (7) can be written as

$$d_i = A_{si} x, \quad i = 1, 2, \ldots, N \tag{10}$$

where A_{si} is the strain model matrix, which is given in (11) shown at the bottom of this page. The unknown vector $x = [d_e\ d_n\ d_u\ \epsilon_{11}\ \epsilon_{12}\ \epsilon_{13}\ \epsilon_{22}\ \epsilon_{23}\ \epsilon_{33}\ \omega_1\ \omega_2\ \omega_3]^T$. As shown in Fig. 2(a), if we treat discrete GNSS points as EPs and use simple LS, the 3-D interpolation deformations of the target point or even the entire grid point with the same resolution as InSAR can be obtained [22].

Before obtaining the optimal 3-D deformations, the variance components of the five observations, that is, GNSS east, north, up, ascending InSAR, and descending InSAR, should be estimated first. However, for a single point, the observation vector y [see (4)] contains only five elements, which is not enough to estimate the variance components of each observation. Liu *et al.* [4] proposed to use a grid strain model to create some virtual observations to increase redundancy. This time, the EPs will become the surrounding points in a regular window centered on the target point, as shown in Fig. 2(b). N is the number of pixels in the window. Then, (4) and (10) can be combined into

$$y_i = (A_{gi} \cdot A_{si}) x = A_i x, \quad i = 1, 2, \ldots, N. \tag{12}$$

If residual errors are taken into account, (12) can be written as a new functional model

$$\underset{5S\times 1}{E\{y\}} = \underset{5S\times 12}{A} \cdot \underset{12\times 1}{x} \tag{13}$$

and (5) becomes a new stochastic model

$$\underset{5S\times 1}{D\{y\}} = \underset{k\times k}{Q_y} = \sum_{i=1}^{k} \sigma_i^2 Q_i. \tag{14}$$

C. IAUE

Liu *et al.* [4] used the famous HVCE method to estimate the variance components of InSAR and MAI for ascending and descending orbits. The disadvantages of HVCE are that its estimated variance components may be negative and difficult to converge [12]. There are many reasons for negative

$$A_{si} = \begin{bmatrix} 1\ 0\ 0 & \triangle p_{ie} & \triangle p_{in} & \triangle p_{iu} & 0 & 0 & 0 & 0 & \triangle p_{iu} & -\triangle p_{in} \\ 0\ 1\ 0 & 0 & \triangle p_{ie} & 0 & \triangle p_{in} & \triangle p_{iu} & 0 & -\triangle p_{iu} & 0 & \triangle p_{ie} \\ 0\ 0\ 1 & 0 & 0 & \triangle p_{ie} & 0 & \triangle p_{in} & \triangle p_{iu} & \triangle p_{in} & -\triangle p_{ie} & 0 \end{bmatrix} \tag{11}$$

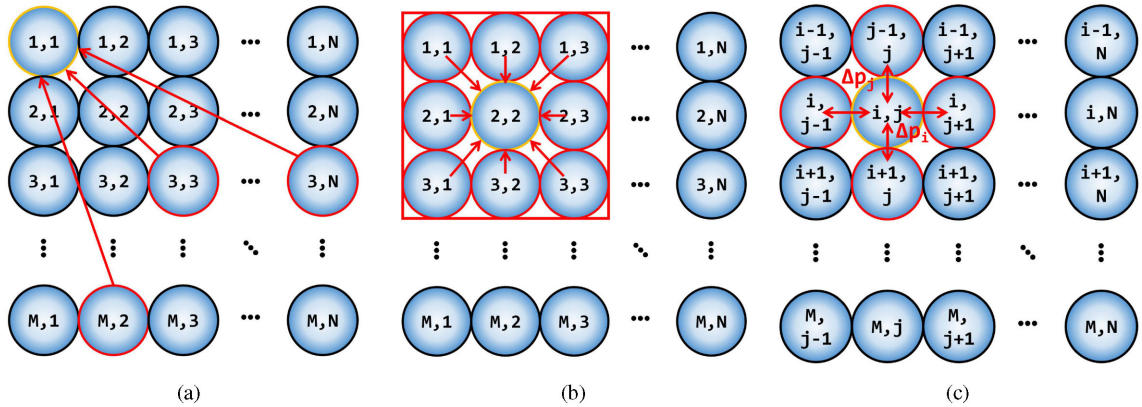

Fig. 2. (a) Pixel representation of GNSS interpolation implemented by grid strain. (b) Pixel representation of SM-VCE performed by grid strain. (c) Pixel representation of LSC strategy.

variances, such as incorrect variance component model, low redundancy of function model, poorly chosen initial variance components, etc. [16]. Negative variance components may result in a nonpositive-definite covariance matrix Q_y, which cannot be physically interpreted.

We propose to use IAUE to estimate the variance components. The concept of IAUE was developed by Hsu [23] and has been proved to be a superior alternative VCE method than the previous HVCE or minimum norm quadratic unbiased estimation [24] due to its many characteristics. Although IAUE provides a biased estimator, it can converge to an approximately unbiased point through multiple iterations [25]. The advantages of IAUE are that it can provide nonnegative variance components and can quickly converge. Instead of estimating variance components directly, IAUE focuses on obtaining estimations for variance factors. After the variance factors have been satisfactorily estimated, the corresponding variance components are computed [18].

In the practical application of IAUE, the observed quantities y are classified into k groups, and for each group, only a single variance component is to be estimated. In our model, $k = 5$. To perform IAUE, $\tilde{\sigma}_i^2$ is assumed to be the initial estimate of σ_i^2. The true variance σ_i^2 can be related to the initial estimate by an unknown factor f_i such that

$$\sigma_i^2 = f_i \tilde{\sigma}_i^2, \quad i = 1, 2, \ldots, k. \tag{15}$$

The covariance matrix of the observation vector y then becomes

$$Q_y = \sum_{i=1}^{k} f_i B_i = \begin{bmatrix} f_1\tilde{b}_1 & 0 & 0 & \cdots & 0 \\ 0 & f_2\tilde{b}_2 & 0 & \cdots & 0 \\ \cdots & \cdots & \cdots & \cdots & \cdots \\ 0 & 0 & \cdots & \cdots & f_k\tilde{b}_k \end{bmatrix} \tag{16}$$

where $B_i = \tilde{\sigma}_i^2 Q_i, \tilde{b}_i = \tilde{\sigma}_i^2 I_i (i = 1, 2, \ldots, k; I_i$ is a unit matrix) is a diagonal matrix associated with group i.

According to [18], the working equations of IAUE are

$$f_i = \frac{y^T W B_i W y}{tr(W B_i)}, \quad i = 1, 2, \ldots, k \tag{17}$$

$$W = P - PA(A^T PA)^{-1} A^T P \tag{18}$$

or the approximate expression [23]

$$f_i \simeq \frac{[r_i]}{y^T W B_i W y}, \quad i = 1, 2, \ldots, k \tag{19}$$

$$R = I - A(A^T PA)^{-1} A^T P \tag{20}$$

where weight matrix $P = Q_y^{-1}$, $[r_i]$ is the sum of the diagonal elements of group i in R. In general, to operate the IAUE, an iterative process is necessary. We start with an initial assumption, usually the identity matrix. As the iteration progresses, the variance factors will be continuously improved. When the vector of variance factors approaches the unit vector, the iteration is terminated. It can be easily seen that, according to working (17) and (19), IAUE will never produce negative variance components. Horn *et al.* [10] pointed out that after a few iterations, the initial estimates will gradually approach unbiased, even if the ideal condition is not met. Therefore, IAUE is called "Almost Unbiased."

Consequently, *a posteriori* variance of unit weight can be obtained by

$$\hat{\sigma} = \frac{1}{5 * N - 12} \sum_{1}^{k} [r_i] f_i. \tag{21}$$

Equation (21) indicates that $\hat{\sigma}$ will become 1, with the variance factors vector converging to unity. This is a unique feature of the IAUE technique. Therefore, $\hat{\sigma}$ can be used as a good iteration termination indicator

$$|\hat{\sigma} - 1| \leq \delta \tag{22}$$

where δ denotes the threshold value of the criterion, which is a small value close to zero. In addition, Förstner [26] points out that group redundancy plays an important role, affecting the convergence of variance factors and δ. Generally speaking, the greater the group redundancy, the faster the convergence and the higher the stability.

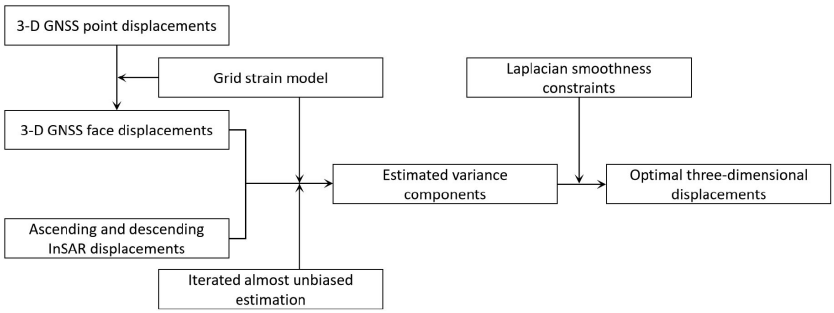

Fig. 3. Flowchart to implement the IAUE-LSC strategy.

D. LSC

In multisource data fusion, heterogeneous data sources usually have different errors, which may result in a large condition number of a normal matrix, thereby amplifying the estimation errors and leading to instability in the solution, demonstrating an ill-posed problem [27]. In addition, the combination of formula (12) makes the size of the design matrix A even larger, which worsens the ill-posed problem of the observation (4) itself. In the simulation part, the instability of the solutions caused by the error ratio of different data will be discussed.

To avoid the instability of the 3-D optimal solutions and avoid the significant difference in the size and direction of the displacements of adjacent pixels, we propose to use the Laplacian smooth constraint [28], [29]. Since the displacement and strain fields are finite [19], some kinds of smoothness among adjacent pixels can be assumed. The Laplace second-order differential operator is

$$\nabla^2 x = 0. \tag{23}$$

For a given point $P_{(i,j)}$, as shown in Fig. 2(c), the smoothness equation for $P_{(i,j)}$ is written as follows:

$$\frac{(x_{(i+1,j)} - x_{(i,j)}) - (x_{(i,j)} - x_{(i-1,j)})}{\triangle p_j^2} + \frac{(x_{(i,j-1)} - x_{(i,j)}) - (x_{(i,j)} - x_{(i,j+1)})}{\triangle p_i^2} = 0 \tag{24}$$

where $x_{i,j}$ is the displacements and strain parameters in the ith row and jth column point and $\triangle p_j^2$ and $\triangle p_i^2$ are the distances between adjacent pixels, as shown in Fig. 2(c). For convenience, we rewrite (24) as follows:

$$Mx = 0 \tag{25}$$

where M is the Laplacian second-order smoothness matrix and its dimension is 12×12. If the vector of 0 on the right of (25), which, corresponding to the second-order derivatives of the displacements, is considered virtual observations, the weight matrix of the real and virtual measurements can be written as follows:

$$P = \begin{bmatrix} P_1 & 0 \\ 0 & P_2 \end{bmatrix} = \begin{bmatrix} Q_y^{-1} & 0 \\ 0 & \lambda I \end{bmatrix} \tag{26}$$

where the Lagrange multiplier λ determines the weight of smoothing and called smoothing factor. Without considering the residual vector, after adding the smooth constraints, the function model (13) can be rewritten as

$$\begin{bmatrix} y \\ 0 \end{bmatrix} = \begin{bmatrix} A \\ M \end{bmatrix} x. \tag{27}$$

The LS solution of (27) is

$$\hat{x} = (A^T P_1 A + \lambda M^T M)^{-1} A^T P_1 y. \tag{28}$$

The smoothing factor's choice is relatively simple, and some methods have been proposed to determine it. The convenient L-curve method [30] is adopted in this article. Fig. 3 indicates the flowchart for implementing the IAUE-LSC strategy. The input data of the system are the GNSS 3-D displacements and the unwrapped deformation maps of InSAR ascending and descending orbits in the interested region, and without *a priori* variance components, the final optimal 3-D solutions can be output. It is worth noting that the input data can also be the deformation data obtained by other techniques, such as MAI, offset tracking, and leveling.

III. Experiments and Discussion

A. Simulated Case

In order to verify the effectiveness of the proposed method, a simple 3-D optimization simulation experiment is carried out first. The Mogi model [31] can calculate the analytical solution for surface deformation due to a point source in an elastic half space. It is widely used to simulate ground deformation produced by local perturbation like volcanic magma chamber. It computes displacements, tilts, and strain in a polar space, due to a volume variation at depth or an isotropic pressure variation in a spherical source [31].

As shown in Fig. 4, we use Mogi model to simulate 3-D surface deformation maps on a 500 m $\times$ 500 m grid, in which the displacements of east–west and north–south range from -7 to 7 cm and the up–down range from -18 to 0 cm. In our simulation experiments, relatively idealized Gaussian errors are added, although InSAR and GNSS are usually contaminated with other more complex noises [32], [33]. In general, the vertical accuracy of GNSS is lower than the horizon. Therefore, Gaussian noises with a mean value of 0 and a standard deviation

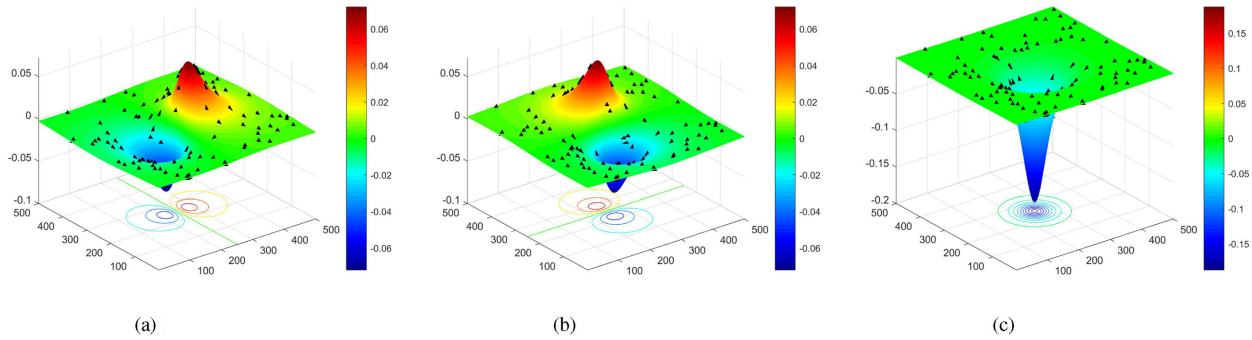

(a) (b) (c)

Fig. 4. Simulated 3-D surface deformation modeled by Mogi. Black triangles represent 100 GNSS points, which are randomly selected. The units of displacement and position are meter. (a) East–west (m). (b) North–south (m). (c) Up–down (m).

TABLE I
COMPARISON OF HVCE AND IAUE

Methods	HVCE			IAUE		
Windows size / Iteration	3×3	5×5	7×7	3×3	5×5	7×7
1	4.666×10^{-6} 4.242×10^{-7} -7.308×10^{-6} 1.489×10^{-4} 7.937×10^{-5}	1.269×10^{-6} 9.805×10^{-8} 4.093×10^{-7} 1.138×10^{-4} 9.384×10^{-5}	6.899×10^{-7} 1.309×10^{-7} 5.729×10^{-7} 1.173×10^{-4} 8.619×10^{-5}	9.011×10^{-6} 1.617×10^{-5} 2.094×10^{-5} 1.836×10^{-5} 2.401×10^{-4}	3.527×10^{-5} 2.893×10^{-5} 1.156×10^{-4} 5.819×10^{-5} 2.991×10^{-4}	2.634×10^{-5} 6.619×10^{-5} 3.618×10^{-5} 4.051×10^{-5} 3.359×10^{-5}
2	———	-2.689×10^{-6} -2.739×10^{-6} -1.455×10^{-6} 0.132 0.087	1.374 0.381 1.687 0.113 0.052	1.420 1.294 1.295 0.938 0.869	0.609 0.682 0.840 0.873 1.014	0.974 1.028 0.981 1.001 1.000
3	———	———	0.614 0.373 1.207 0.100 0.083	0.093 0.944 0.912 0.150 0.952	0.952 1.000 0.994 0.972 0.994	1.004 0.998 0.999 0.990 1.010

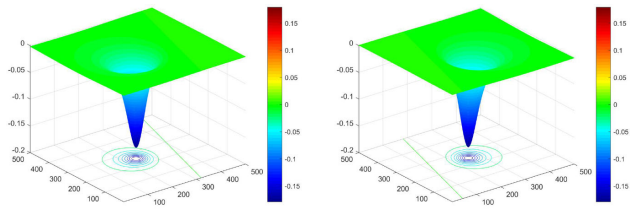

(a) (b)

Fig. 5. Synthetic (a) ascending and (b) descending InSAR data. The units of displacement and position are meter.

of 0.4 and 0.8 cm are added to the horizontal and vertical directions, respectively. Then, 100 points are randomly selected as GNSS points, as shown by the black triangle in Fig. 4, and the simulated deformation and noise are used as GNSS deformation and noise. To simulate InSAR data, we convert the 3-D displacement into the displacement in LOS direction d_{los} using (3). $[0.34 \ -0.095 \ 0.935]$ and $[-0.34 \ 0.095 \ 0.935]$ serve as the projection vectors for the ascending and descending InSAR data, respectively. The synthesized InSAR data are shown in Fig. 5. The grid strain method is used to make 100 randomly selected GNSS points to the same spatial resolution as InSAR for the next step of fusion. The 3-D results are shown in Fig. 6(a)–(c).

On an arbitrarily selected EP, the performance of IAUE and HVCE is first compared, as shown in Table I. The five values corresponding to HVCE and IAUE are the unit weight variances and variance factors of GNSS east, north, up, and InSAR ascending and descending orbits, respectively. By changing the size of the window around the EP, the convergence and iteration of HVCE and IAUE can be observed. When few pixels (3×3) around the target point are combined to perform the two SM-VCE methods described above, that is, when the observed redundancy is insufficient, the results of HVCE tend to appear negative variance components. Only when the size of the window keeps increasing, the result of HVCE can avoid negative variances and converge. In other words, HVCE can obtain more reliable results only when the observed redundancy is large enough. Due to the nonnegative characteristics mentioned above, IAUE can obtain nonnegative variance components even when the windows size is small. However, like other VCE methods, redundancy has a great impact on IAUE [26]. To further explore the performance of IAUE, the variance factors, variance components, and variance of the unit weight for the first six iterations are shown in Table II. When the size of the window is 3×3, although IAUE can still give a nonnegative variances estimate, it needs more steps to achieve convergence. Moreover, compared with the larger window ($\geq 9 \times 9$), the estimated variance components seem unreliable. When the window size is 9×9 or larger, the convergence ability of IAUE is impressive; the variance factors can be very close to the unity after two or three iterations basically. In addition, the influence of different redundancy on the accuracy

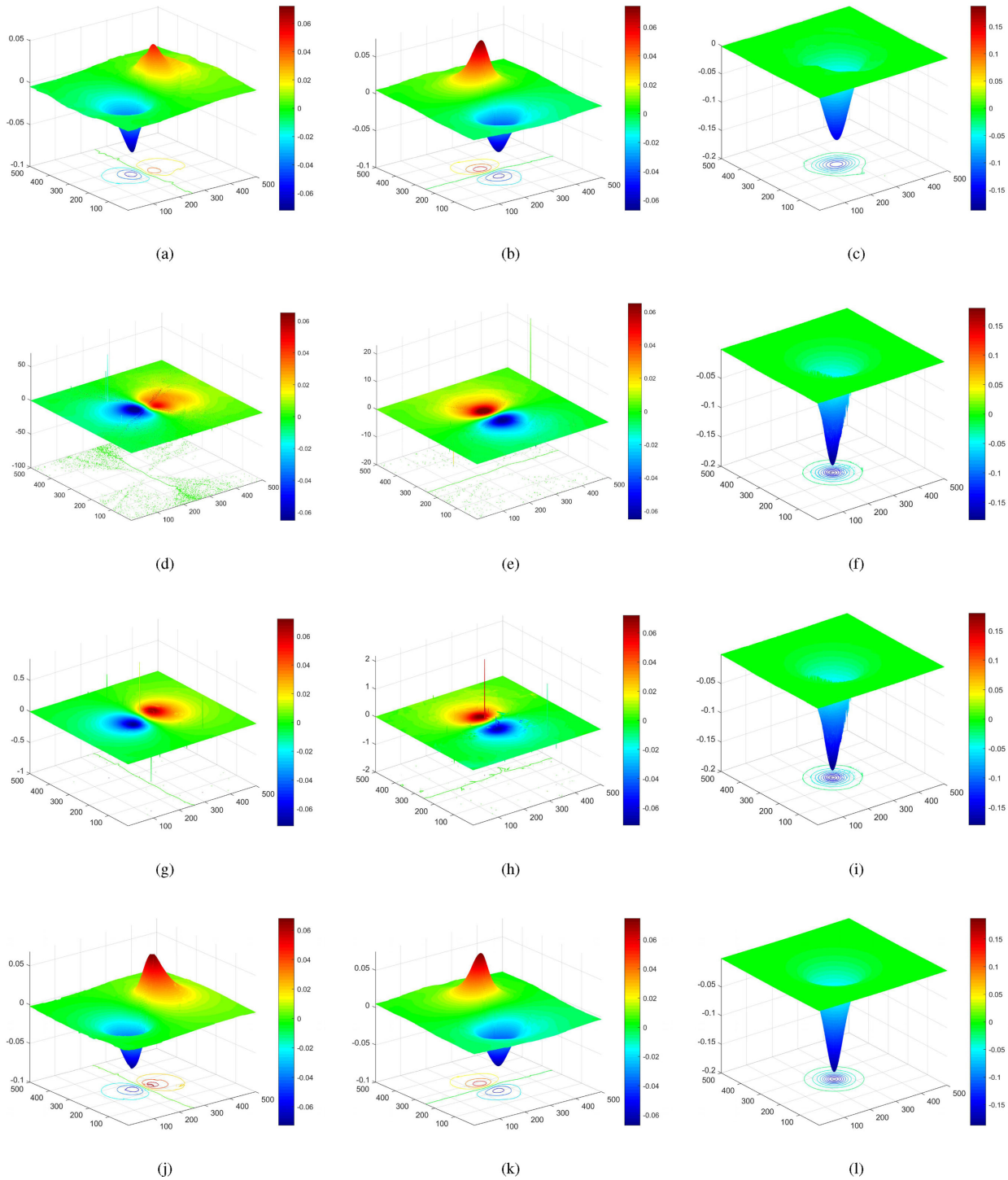

Fig. 6. (a)–(c) 3-D deformation results of grid strain model. Optimized 3-D deformation maps acquired by (d)–(f) WLS, (g)–(i) IAUE, and (j)–(l) IAUE-LSC when SDR $> 10^4$. The units of displacement and position are meter.

of the final 3-D optimal deformations should also be considered. In order to determine the number of surrounding pixels to operate IAUE, a comparison experiment is performed, as shown in Fig. 7. As the size of window increases, root-mean-square errors (RMSEs) for the east, north, and up decrease and gradually stabilize, but the cost of time also increases. To balance time and accuracy, a 9×9 window is selected.

Then, we adjust the standard deviation ratio (SDR) between GNSS and InSAR to perform multiple comparative experiments applying LS, WLS, IAUE alone, and combined IAUE-LSC, respectively. The Gaussian standard deviations serve the weights for WLS, and RMSEs are adopted to evaluate the performance of different methods. To simplify the experimental process, we only change the standard deviations of InSAR. Fig. 8 indicates

TABLE II
VARIANCE FACTORS, ESTIMATED VARIANCE COMPONENTS, AND VARIANCE OF UNIT WEIGHT FOR IAUE

Windows size	3×3			9×9			13×13		
Iteration	f_i	σ_i^2	$\hat{\sigma}$	f_i	σ_i^2	$\hat{\sigma}$	f_i	σ_i^2	$\hat{\sigma}$
1	9.01e-6 1.62e-5 2.09e-5 1.84e-5 2.40e-4	9.01e-6 1.62e-5 2.09e-5 1.84e-5 2.40e-4	6.46e-6	2.42e-5 6.86e-5 3.72e-5 4.36e-5 3.93e-5	2.42e-5 6.86e-5 3.72e-5 4.36e-5 3.93e-5	4.29e-5	2.53e-5 6.76e-5 3.87e-5 4.23e-5 3.83e-5	2.53e-5 6.76e-5 3.87e-5 4.23e-5 3.83e-5	4.32e-5
2	1.42 1.29 1.29 0.93 0.86	1.27e-5 2.09e-5 2.71e-5 1.72e-5 2.08e-4	1.21	1.00 0.99 0.99 1.00 0.99	2.43e-5 6.84e-5 3.71e-5 4.35e-5 3.92e-5	1.00	1.00 0.99 0.99 1.00 0.99	2.42e-5 6.86e-5 3.72e-5 4.36e-5 3.93e-5	1.00
3	0.09 0.94 0.91 0.15 0.95	1.24e-6 1.98e-5 2.48e-5 2.59e-6 1.98e-4	0.73	0.99 1.00 0.99 0.99 1.00	2.43e-5 6.86e-5 3.68e-5 4.32e-5 3.94e-5	1.00	1.00 0.99 0.99 1.02 0.99	2.44e-5 6.76e-5 3.72e-5 4.36e-5 3.93e-5	1.01
4	4.85 0.80 0.91 3.55 1.12	6.03e-6 1.60e-5 2.27e-5 9.20e-6 2.22e-4	2.04	0.99 1.00 0.99 1.01 1.00	2.42e-5 6.87e-5 3.65e-5 4.36e-5 3.96e-5	1.00	1.00 0.99 0.99 1.00 0.99	2.42e-5 6.86e-5 3.72e-5 4.36e-5 3.93e-5	0.99
5	0.87 0.89 1.04 1.02 1.01	5.30e-6 1.44e-5 2.26e-5 9.42e-6 2.26e-4	1.06	1.00 0.99 1.01 0.99 1.00	2.44e-5 6.86e-5 3.72e-5 4.33e-5 3.94e-5	1.00	1.00 0.99 1.00 1.00 1.00	2.44e-5 6.85e-5 3.72e-5 4.34e-5 3.93e-5	1.00
6	0.91 0.97 1.18 0.91 1.02	5.22e-6 1.32e-5 2.16e-5 9.69e-6 2.13e-4	1.06	1.00 0.99 1.01 1.00 1.00	2.46e-5 6.86e-5 3.72e-5 4.38e-5 3.89e-5	1.00	1.00 1.00 0.99 1.01 1.00	2.46e-5 6.83e-5 3.71e-5 4.36e-5 3.92e-5	1.00

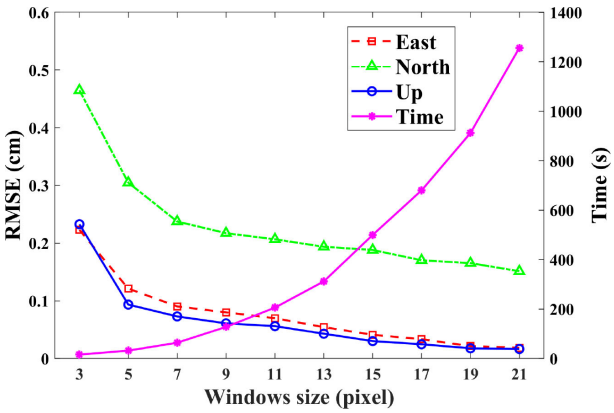

Fig. 7. Experiment to determine the optimal windows size. As the size of the windows around the target point changes, the RMSEs of the 3-D deformations acquired by IAUE changes.

the changes in RMSE of LS, WLS, IAUE, and IAUE-LSC as the SDR changes. A few interesting discoveries can be obtained from our simulated experiments. First of all, the RMSE of LS shows great instability and is most affected by the standard deviation of InSAR. When the relative error of InSAR increases, especially when SDR $\leq 10^{-1}$, the error of LS increases sharply. As the SDR increases, that is, the relative error of the InSAR becomes small, the performance of the LS becomes stable. Second, WLS, IAUE, and IAUE-LSC improve the accuracy better than normal LS in east and up directions and exhibit better stability when the relative error of InSAR increases clearly. However, in the north, LS seems to perform better than other methods. We speculate that this is due to the fact that GNSS has the largest impact on the north. As the relative error of GNSS increases, the weight decreases, while InSAR becomes relatively stable, thus making LS perform better. In general, it is very effective to adopt a weighting method for different data. Furthermore, the performance of IAUE and WLS is very close. This fully illustrates that IAUE can successfully extract the weights of observational measurements without *a priori* variance. Moreover, when SDR $> 10^4$, the errors of WLS and IAUE increase sharply in the east and north directions, as shown in Fig. 8(a) and (b). Fig. 6(d)–(f) and (g)–(i), respectively, indicate the 3-D optimization results obtained by applying WLS and IAUE when SDR $> 10^4$, showing great errors and spatial discontinuities. From Fig. 8, the error of IAUE seems to be greater than that of WLS. This happens because, for simulation purposes, the standard deviations of GNSS and InSAR are accurately known. And one could get the best linear unbiased estimation by taking the weight matrix to be the inverse of the variance matrix to perform WLS [16]. However, IAUE-LSC still achieves high precision and stable results [see Fig. 6(j)–(l)], showing robustness against the inverse effects of the ill-posed normal matrix.

B. Real Case

At 21:32 on May 4, 2018 (UTC), an earthquake with a magnitude of 5.4 struck the island of Hawaii. About an hour later, a major earthquake with a magnitude of 6.9 occurred.[1] The earthquakes prompted the Kilauea volcano to erupt overnight,

[1][Online]: Available: https://earthquake.usgs.gov/earthquakes/eventpage/hv7011655 6/executive

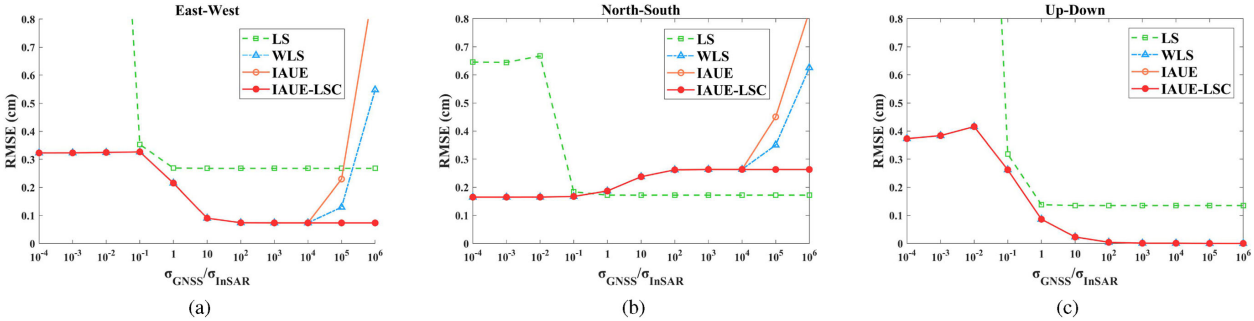

Fig. 8. Different performances of LS, WLS, IAUE, and IAUE-LSC, by adjusting the SDR.

TABLE III
INTERFEROMETRIC PAIRS USED IN THE STUDY

Date of master image	Date of slave image	Polarization	Direction	Perpendicular baseline (m)
20 April 2018	8 May 2018	VV	Ascending	-33.3934
23 April 2018	5 May 2018	VV	Descending	83.5911

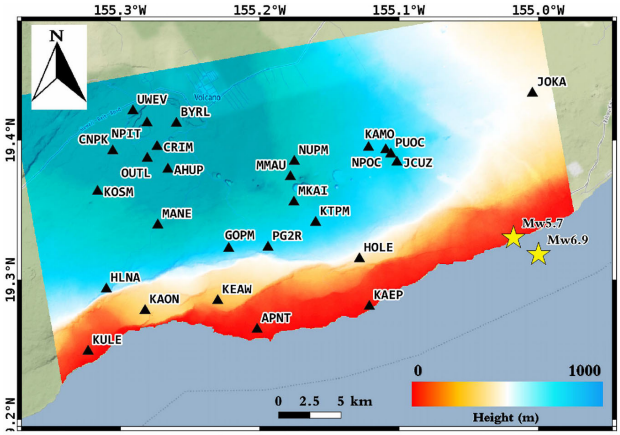

Fig. 9. Topographic map of the study area. It is obtained by the SRTM with a resolution of 90 m. The four characters next to the arrow indicate the name of the GNSS station. The black triangle represents the position of GNSS, and the four characters around it represent the name of GNSS.

causing lava to flow into residential areas. As listed in Table III, two pairs of Sentinel-1 A satellites' ascending and descending orbit images are used to extract the displacements in the LOS direction. The 90-m resolution SRTM data are used to remove the terrain phase. The topography of the study area is shown in Fig. 9. Differential interferograms of the ascending and descending orbits [see Fig. 10(a) and (b)] show interference fringes that can detect significant surface displacements caused by the earthquakes. Based on the minimum cost flow algorithm, the true phases of two pairs of interferograms are extracted and converted into displacements in the LOS direction.

Fig. 11(a) and (b) indicates the LOS displacements obtained using the ascending and descending InSAR. It can be seen that the earthquakes triggered huge displacements along the East Rift Zone of Kilauea Volcano, especially around the Pu'u'Ō'ō caldera. In the northwest of the study area, a displacement of approximately 30 cm due to the eruption of Kilauea volcano is also observed. The maximum displacement observed by the ascending InSAR is about 60 cm, and that of the descending orbit is about 20 cm. One advantage of the 2018 Hawaii earthquakes is that the GNSS continuous observation station in the earthquake area is very short from the deformation center, which is very suitable for joint GNSS and InSAR observation. The time series of the 27 GNSS stations are provided by the Nevada laboratory.[2] The displacements of the 27 GNSS stations in the study area from April 20 to May 8 are also shown in Fig. 11 with purple arrows. The NPIT station nearest to Kilauea volcano has a significant post-earthquake displacement. However, there is no significant movement at the sites 4 km away from the volcano, indicating that the large-scale crustal movement caused by the volcanic eruption after the earthquakes is limited to a small range near the crater.

The 3-D optimal deformation maps are extracted by applying our proposed method, as shown in Fig. 12(a), (c), and (e). A clear southeastward movement, that is, a seaward trend is indicated in Fig. 12(a) and (c), consistent with the direction indicated by GNSS in Fig. 11. On the west side, the deformation is mainly distributed near the Kilauea crater, while on the east side, it mainly occurs in the Pu'u'Ō'ō area and extends toward the sea. Overall, the displacements on the west side are significantly smaller than that on the east side. The ground deformation caused by the collapse of Pu'u'Ō'ō crater continued to spread eastward and invaded into the densely populated lower ERZ (east of GNSS station JOKA) [34].

In addition, we have extracted the 3-D deformation maps using the traditional WLS method, as shown in Fig. 12(b), (d), and (f). The errors of InSAR are calculated by (2). The general deformation trend is consistent with that obtained by IAUE-LSC [see Fig. 12(a), (c), and (e)]. However, it can be clearly seen that in the Pu'u'Ō'ō caldera area, that is, near the GNSS stations NPOC and JCUZ, there are obvious disturbances in east–west and up–down components. In the north–south component, the disturbances occur in other areas, mainly along the coast and west of Kilauea volcano [35]. The numerical results of IAUE-LSC and WLS, 3-D results along a profile marked AB (blue line in Fig. 12), are shown in Fig. 13. It can be seen that along

[2][Online]: Available: http://geodesy.unr.edu/

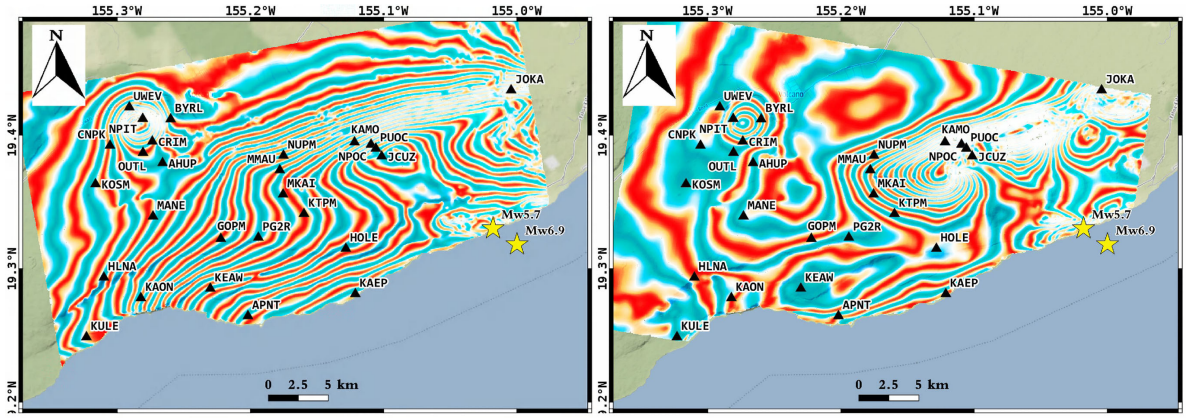

(a) (b)

Fig. 10. Coseismic wrapped interferogram of the 2018 Hawaii earthquakes. (a) Ascending track. (b) Descending track. Each fringe corresponds to 2.8 cm of LOS motion. The black triangle represents the position of the GNSS, and the four characters around it represent the name of GNSS station.

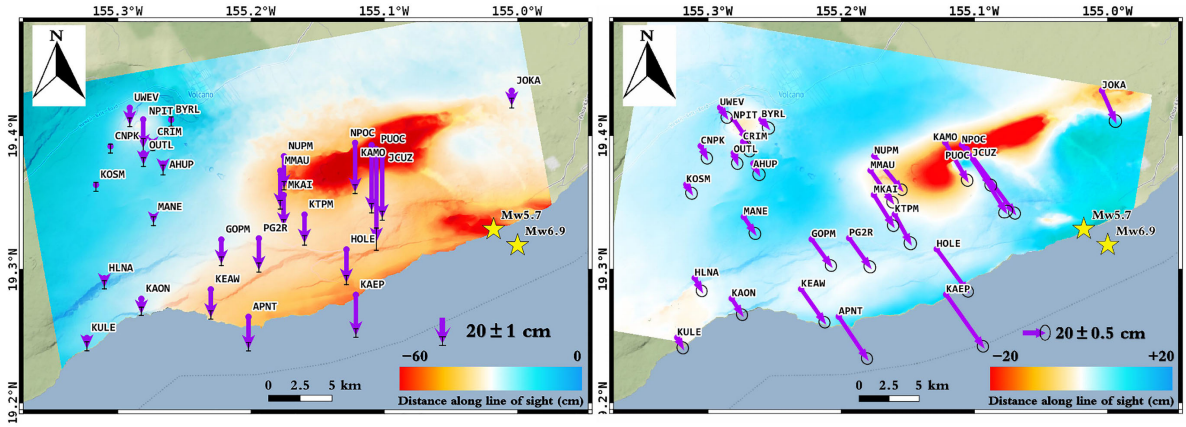

(a) (b)

Fig. 11. InSAR deformation maps. (a) Ascending track. (b) Descending track. GNSS sites with displacement vectors are indicated by purple arrows. The four characters next to the arrow indicate the name of GNSS station. The black ellipses and the vertical lines represent the horizontal and vertical errors, respectively.

the line AB, the results of the traditional WLS have a lot of disorder and instability in the east–west and vertical directions. The north–south direction results obtained by WLS performed well along AB, but poorly along the southeast coast and west of the Kilauea volcano [see Fig. 12(c) and (d)]. This shows that the poor solutions caused by heterogeneous error sources do not always appear in the same area and also proves the necessity of using LSC.

To further compare the results of the two weighting methods, the standard deviations of the five observations along the profile AB obtained by traditional HVCE and IAUE methods are compared, as shown in Fig. 14. It can be seen that using prior variances to determine the weights has great limitations. It obtains the weight of the GNSS by interpolating the positioning errors of the GNSS to the same grid as InSAR and calculates the weights of InSAR by the coherence coefficient of InSAR [see (1)]. On the one hand, without considering InSAR and GNSS as the overall observation vector, it is straightforward to produce weights that are too different, making the normal matrix ill-conditioned and the solution unstable, as discussed in the simulation experiment. It must be realized that the design matrix used in Fig. 14(a) is the simple A_g in (4) and still makes the condition number of normal matrix reach the order of 10^7. On the other hand, using only coherence to estimate the standard deviations of InSAR is highly unreasonable. First of all, how to calculate the coherence accurately has been a problem [32], [36]. Second, the error of InSAR observation is also affected by spatiotemporal uncorrelated noises and atmospheric noises, which is more difficult to be estimated [33]. Fig. 14(b) shows the variance components of GNSS and InSAR that are successfully estimated by IAUE for the first time. On the one hand, its rationality lies in that due to the randomness of variance; it presents a "noise-like" spatial distribution. On the other hand, when extending from A to B, the standard deviations estimated by IAUE tend to increase first and then decrease. This is because the middle of the profile line AB is the seismic center zone with great errors, which can be seen from Fig. 12. In addition, IAUE's results show lower errors of GNSS east and north directions than those of the vertical direction and InSAR. This is determined by the characteristics of the different sensors and is well reflected in our results. However, Fig. 14(b) also shows that the condition number of the normal matrix obtained by our results is still huge.

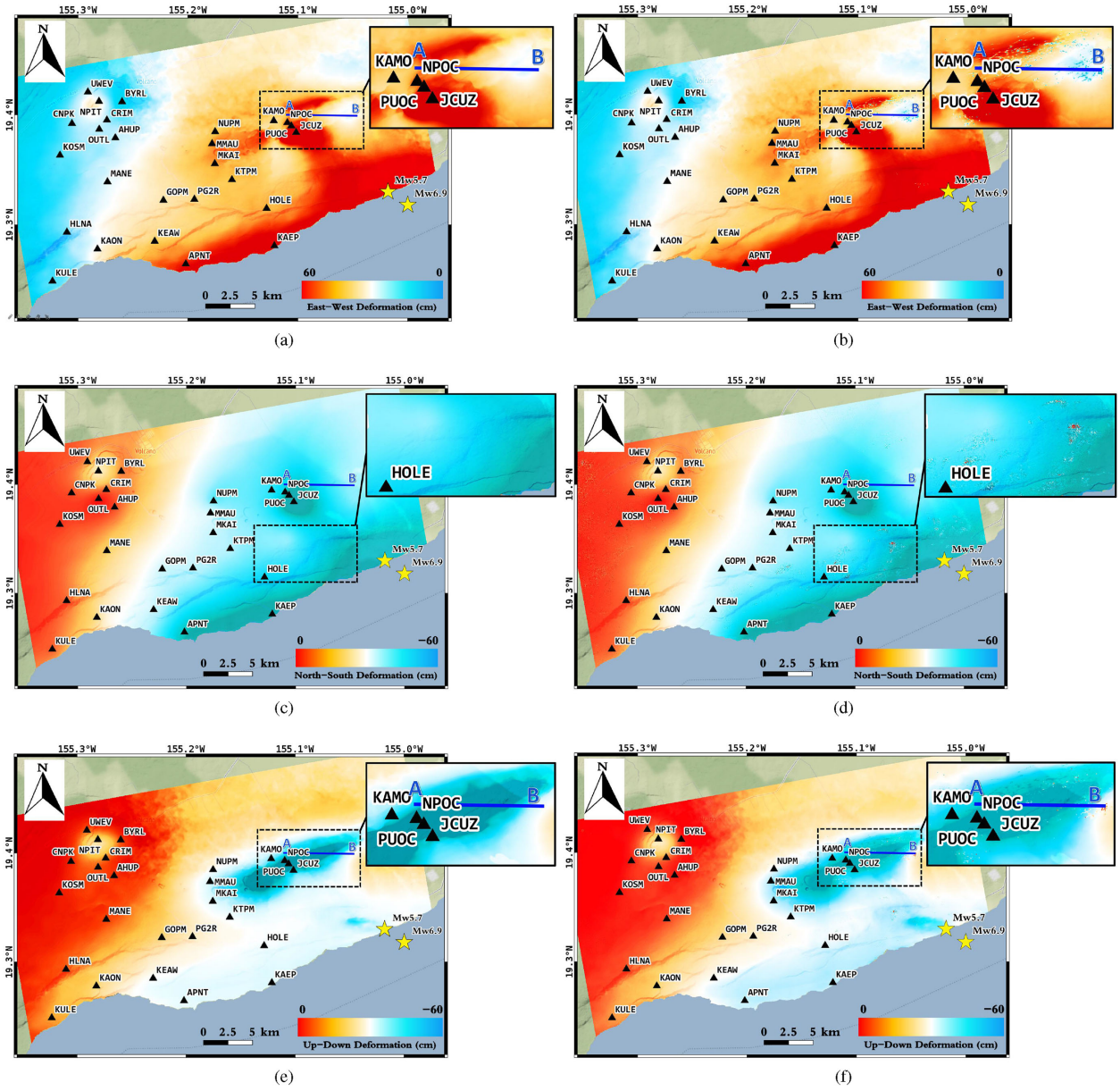

Fig. 12. Optimized 3-D deformation maps calculated by IAUE-LSC [(a), (c), and (e)] and WLS [(b), (d), and (f)] methods, respectively. (Top) east–west component. (Middle) north–south component. (Bottom) up–down component. GNSS sites are represented by black triangles. The blue solid line shows the location of profile AB.

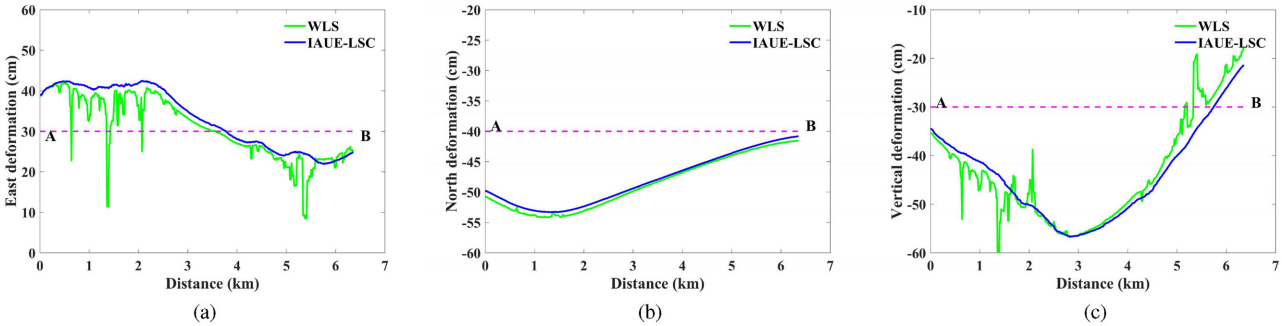

Fig. 13. (a)–(c) IAUE-LSC and WLS deformation along the profile AB.

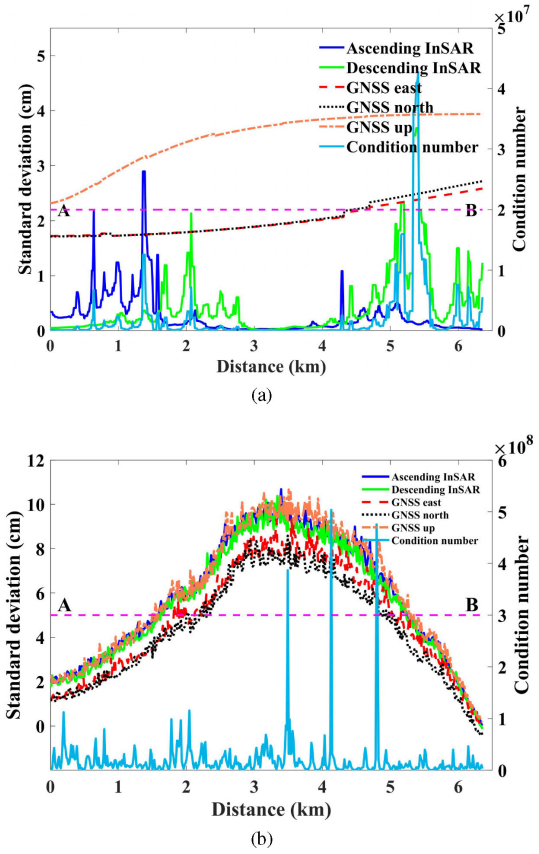

Fig. 14. Variance components along the profile AB, estimated by (a) WLS and (b) IAUE.

TABLE IV
RMSEs OF ENU FOR WLS, IAUE, AND IAUE-LSC METHOD

	East (cm)	North (cm)	Up (cm)
WLS	6.25	9.01	11.60
IAUE	3.67	6.24	3.91
IAUE-LSC	1.38	5.92	2.23

This is mainly influenced by the design matrix A_s [see (10) and (13)]. Therefore, although the variance components obtained by IAUE are already at the same level, that is, the SDR is close to 1, the stability of the solutions still needs to be achieved through LSC.

Furthermore, Table IV lists the RMSEs of the 3-D solutions obtained using WLS, IAUE alone, and combined IAUE-LSC methods. It can be seen that the improvements of IAUE compared to WLS are obvious, which are 2.58, 2.77, and 7.69 cm, respectively. It shows that accurate weight determination has an important influence on the final solution. Moreover, compared with the IAUE method alone, the combined IAUE-LSC also has improvements of 2.29, 0.32, and 1.68 cm, which indicates that LSC has the effect of stabilizing the final solutions.

IV. CONCLUSION

Accurate 3-D surface deformations are of great significance for the investigating of geohazards. This article describes a new method, termed as IAUE-LSC, to improve the process of solving 3-D deformation. Our research has discovered the following facts. The IAUE variances estimator can overcome the problem of the negative variances and guarantee a positive value for the estimation. By using the IAUE, the reliable variance components of the observation vector can be obtained, which further improves the accuracy of 3-D optimal deformations. Moreover, the ill-posed system, which is introduced by heterogeneous data errors and strain model, can yield reliable results if the displacements between adjacent pixels are limited, such as our proposed LSC. It is worth noting that the proposed method can also input the deformation data obtained through other techniques, such as MAI, offset tracking, and leveling by establishing observation vector and design matrix A_g similar to (4).

ACKNOWLEDGMENT

The authors would like to thank the European Space Agency for providing Sentinel-1 data and the Nevada laboratory for providing GNSS time series on the Island of Hawaii.

REFERENCES

[1] Y. Yun *et al.*, "Application of spaceborne interferometric synthetic aperture radar to geohazard monitoring," *J. Radars*, vol. 9, no. 1, pp. 73–85, 2020.
[2] P. F. Ji, X. L. Lv, F. J. Dou, and Y. Yun, "Fusion of GPS and InSAR data to derive robust 3D deformation maps based on MRF L1-regularization," *Remote Sens. Lett.*, vol. 11, no. 2, pp. 204–213, 2020.
[3] S. Samsonov and K. Tiampo, "Analytical optimization of a DInSAR and GPS dataset for derivation of three-dimensional surface motion," *IEEE Geosci. Remote Sens. Lett.*, vol. 3, no. 1, pp. 107–111, Jan. 2006.
[4] J. H. Liu, J. Hu, Z. W. Li, J. J. Zhu, Q. Sun, and J. Gan, "A method for measuring 3D surface deformations with InSAR based on strain model and variance component estimation," *IEEE Trans. Geosci. Remote Sens.*, vol. 56, no. 1, pp. 239–250, Jan. 2018.
[5] J. Hu, Z. Li, X. Ding, J. Zhu, L. Zhang, and Q. Sun, "Resolving three-dimensional surface displacements from InSAR measurements: A review," *Earth-Sci. Rev.*, vol. 133, pp. 1–17, 2014.
[6] S. Samsonov, K. Tiampo, J. Rundle, and Z. Li, "Application of DInSAR-GPS optimization for derivation of fine-scale surface motion maps of Southern California," *IEEE Trans. Geosci. Remote Sens.*, vol. 45, no. 2, pp. 512–521, Feb. 2007.
[7] R. J. Walters, B. Parsons, and T. J. Wright, "Constraining crustal velocity fields with InSAR for eastern Turkey: Limits to the block-like behavior of Eastern Anatolia," *J. Geophys. Res.: Solid Earth*, vol. 119, no. 6, pp. 5215-5234, 2014.
[8] J. Hu, J. J. Zhu, Z. W. Li, X. L. Ding, C. C. Wang, and Q. Sun, "Robust estimating three-dimensional ground motions from fusion of InSAR and GPS measurements," in *Proc. Int. Symp. Image Data Fusion*, 2011, pp. 3–6.
[9] G. Q. Shi, X. F. He, and R. Y. Xiao, "Acquiring three-dimensional deformation of Kilauea's south flank from GPS and DInSAR integration based on the ant colony optimization," *IEEE Geosci. Remote Sens. Lett.*, vol. 12, no. 12, pp. 2506-2510, Dec. 2015.
[10] S. D. Horn, R. A. Horn, and D. B. Duncan, "Estimating heteroscedastic variances in linear models," *J. Amer. Statist. Assoc.*, vol. 70, no. 350, pp. 380-385, 1975.
[11] J. Hu *et al.*, "Measuring three-dimensional surface displacements from combined InSAR and GPS data based on BFGS method," *Chin. J. Geophys.*, vol. 56, no. 1, pp. 117-126, 2013.
[12] P. J. G. Teunissen and A. R. Amiri-Simkooei, "Least-squares variance component estimation," *J. Geodesy*, vol. 82, no. 2, pp. 65-82, Aug. 2007.
[13] H. Mehrabi, B. Voosoghi, M. Motagh, and R. F. Hanssen, "Three-dimensional displacement fields from InSAR through Tikhonov regularization and least-squares variance component estimation," *J. Surv. Eng.*, vol. 145, no. 4, 2019, Art. no. 04019011.
[14] T. Kall, T. Oja, and K. Tänavsuu, "Postglacial land uplift in Estonia based on four precise levelings," *Tectonophysics*, vol. 610, pp. 25–38, 2014.
[15] X. Song, Y. Jiang, X. Shan, and C. Qu, "Deriving 3D coseismic deformation field by combining GPS and InSAR data based on the elastic dislocation model," *Int. J. Appl. Earth Observ. Geoinf.*, vol. 57, pp. 104-112, 2017.

[16] A. R. Amiri-Simkooei, "Non-negative least-squares variance component estimation with application to GPS time series," *J. Geodesy*, vol. 90, no. 5, pp. 451-466, 2016.
[17] T. Fuhrmann and M. C. Garthwaite, "Resolving three-dimensional surface motion with InSAR: Constraints from multi-geometry data fusion," *Remote Sens.*, vol. 11, no. 3, 2019, Art. no. 241.
[18] J. R. Lucas, "A variance component estimation method for sparse matrix application," Nat. Oceanic Atmos. Admin., Rockville, MD, USA, Tech. Rep. NOS 111 NGS 33, 1985.
[19] G. Teza, A. Pesci, and A. Galgaro, "Grid strain and grid strain3: Software packages for strain field computation in 2D and 3D environments," *Comput. Geosci.*, vol. 34, no. 9, pp. 1142-1153, 2008.
[20] M. A. Goudarzi, M. Cocard, and R. Santerre, "GeoStrain: An open source software for calculating crustal strain rates," *Comput. Geosci.*, vol. 82, pp. 1–12, 2015.
[21] F. Guglielmino, G. Nunnari, G. Puglisi, and A. Spata, "Simultaneous and integrated strain tensor estimation from geodetic and satellite deformation measurements to obtain three-dimensional displacement maps," *IEEE Trans. Geosci. Remote Sens.*, vol. 49, no. 6, pp. 1815-1826, Jun. 2011.
[22] F. Guglielmino, G. Nunnari, G. Puglisi, and A. Spata, "SISTEM: A new global approach to obtain three-dimensional displacement maps by integrating GPS and DInSAR data," in *Proc. 'Fringe 2009 Workshop*, 2009, vol. 11, no. 2, p. 5890.
[23] R. Hsu, "An alternative expression for the variance factors in using iterated almost unbiased estimation," *J. Geodesy*, vol. 73, no. 4, pp. 173-179, 1999.
[24] C. Rao, "Estimation of variance and covariance components—MINQUE theory," *J. Multivariate Anal.*, vol. 1, no. 3, pp. 257–275, 1971.
[25] E. Mysen, "On variance component estimation with pseudo-observations," *GEM - Int. J. Geomath.*, vol. 9, no. 2, pp. 317–334, 2018.
[26] W. Förstner, "A method for estimating variance and covariance components," (in German), *Allgemeine Vermessung Nachrichten*, vol. 86, no. 11, pp. 446–453, 1979.
[27] A. N. Tikhonov, "Solution of incorrectly formulated problems and the regularization method," *Sov. Math. Doklady*, vol. 4, pp. 1035–1038, 1963.
[28] S. Jonsson, "Fault slip distribution of the 1999 Mw 7.1 Hector Mine, California, earthquake, estimated from satellite radar and GPS measurements," *Bull. Seismol. Soc. Amer.*, vol. 92, no. 4, pp. 1377–1389, Jan. 2002.
[29] F. Maerten, "Inverting for slip on three-dimensional fault surfaces using angular dislocations," *Bull. Seismol. Soc. Amer.*, vol. 95, no. 5, pp. 1654–1665, Jan. 2005.
[30] P. C. Hansen, "Analysis of discrete ill-posed problems by means of the L-curve," *SIAM Rev.*, vol. 34, no. 4, pp. 561–580, 1992.
[31] K. Mogi, "Relations between the eruptions of various volcanoes and the deformations of the ground surfaces around them," *Earthq. Res. Inst.*, vol. 36, pp. 99–134, 1958.
[32] H. Zebker and K. Chen, "Accurate estimation of correlation in InSAR observations," *IEEE Geosci. Remote Sens. Lett.*, vol. 2, no. 2, pp. 124–127, Apr. 2005.
[33] X. L. Ding, Z. W. Li, J. J. Zhu, G. C. Feng, and J. P. Long, "Atmospheric effects on InSAR measurements and their mitigation," *Sensors*, vol. 8, no. 9, pp. 5426–5448, 2008.
[34] C. A. Neal *et al.*, "The 2018 rift eruption and summit collapse of Kīlauea volcano," *Science*, vol. 363, pp. 367–374, Jan. 2019.
[35] J. Hu, Z. W. Li, Q. Sun, J. J. Zhu, and X.-L. Ding, "Three-dimensional surface displacements from InSAR and GPS measurements with variance component estimation," *IEEE Geosci. Remote Sens. Lett.*, vol. 9, no. 4, pp. 754–758, Jul. 2012.
[36] H. Zebker and J. Villasenor, "Decorrelation in interferometric radar echoes," *IEEE Trans. Geosci. Remote Sens.*, vol. 30, no. 5, pp. 950–959, Sep. 1992.

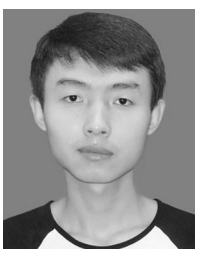

Panfeng Ji received the B.S. degree in measurement and control technology and instrument from Xidian University, Xi'an, China, in 2017. He is currently working toward the Ph.D. degree in signal processing with the Aerospace Information Research Institute, Chinese Academy of Sciences, Beijing, China.

He is currently with the University of Chinese Academy of Sciences, Beijing. His current research interests include interferometric synthetic aperture radar, and its integration with other geodesy technologies on 3-D surface deformation mapping.

Xiaolei Lv (Member, IEEE) received the B.S. degree in computer science and technology and the Ph.D. degree in signal processing from Xidian University, Xi'an, China, in 2004 and 2009, respectively.

From 2009 to 2010, he was with the School of Electrical and Electronic Engineering, Nanyang Technological University, Singapore. From 2011 to 2013, he was with the Department of Civil and Environmental Engineering, Rensselaer Polytechnic Institute, Troy, NY, USA. Since April 2013, he has been a Professor with the Institute of Electronics, Chinese Academy of Sciences, Beijing, China. His main research interests include sparse signal processing, radar imaging (synthetic aperture radar/inverse synthetic aperture radar), interferometric synthetic aperture radar, and ground moving-target indication.

Qi Chen received the master's degree in communication and information systems and the Ph.D. degree in signal and information processing from the Institute of electronics, Chinese Academy of Sciences, Beijing, China, in 2004 and 2007, respectively.

He is currently a Professor with the China Centre for Resources Satellite Data and Application, Beijing. He has authored or coauthored one book and more than ten papers. His research interests include high-resolution synthetic aperture radar (SAR) imaging processing, interferometric SAR data processing, and differential interferometric SAR deformation measurement.

Guangcai Sun (Senior Member, IEEE) received the master's degree in communications engineering from the Xi'an University of Posts and Telecommunications, Xi'an, China, in 2006, and the Ph.D. degree in signal and information processing from Xidian University, Xi'an, in 2012.

He is currently an Associate Professor with the National Laboratory of Radar Signal Processing, and also with the Collaborative Innovation Center of Information Sensing and Understanding, Xidian University. He has authored or coauthored one book and more than 50 papers. His research interests include imaging of several synthetic aperture radar modes, moving target detection, and imaging.

Jingchuan Yao received the M.S. degree in bridge and tunnel engineering and the Ph.D. degree in road and railway engineering from the China Academy of Railway Sciences, Beijing, China, in 2003 and 2008, respectively.

Since August 2008, he has been with the State Key Laboratory of High Speed Railway Track Technology and Beijing Tieke Engineering Inspection Company, Ltd., China Academy of Railway Sciences. He authored or coauthored more than 20 academic papers. His main research interests include railway infrastructure operation and maintenance, bridge dynamic and operational performance evaluation, railway bridge parameter identification and state assessment, and railway and urban rail transit vibration evaluation.

Dr. Yao is the Principal Investigator (PI) or the Co-PI of more than 20 projects supported by the National Science and Technology Support Program of China and the National Natural Science Foundation of China. He has been awarded more than 20 science and technology awards.